Petroleum Science 19 (2022) 990–1006

Contents lists available at ScienceDirect

Petroleum Science

journal homepage: www.keaipublishing.com/en/journals/petroleum-science

Original Paper

Coupling mechanism of THM fields and SLG phases during the gas extraction process and its application in numerical analysis of gas occurrence regularity and effective extraction radius

Hui-Huang Fang [a, b, c, *], Chun-Shan Zheng [b, **], Ning Qi [d], Hong-Jie Xu [a, b, c], Hui-Hu Liu [a, b, c], Yan-Hui Huang [a, c, e], Qiang Wei [b, f], Xiao-Wei Hou [b, g], Lei Li [h], Shuai-Liang Song [i]

[a] State Key Laboratory of Mining Response and Disaster Prevention and Control in Deep Coal Mines, Anhui University of Science and Technology, Huainan, Anhui 232001, China
[b] Institute of Energy, Hefei Comprehensive National Science Center, Hefei, Anhui 230000, China
[c] School of Earth and Environment, Anhui University of Science and Technology, Huainan, Anhui 232001, China
[d] Great Institute of Standardization, China National Institute of Standardization's High Quality and Green Development Innovation R&D Base, Jinan, Shandong 250101, China
[e] State Key Laboratory of Petroleum Resources and Prospecting, China University of Petroleum, Beijing, 102249, China
[f] School of Resources and Civil Engineering, Suzhou University, Suzhou, Jiangsu 234000, China
[g] School of Resources and Environmental Engineering, Hefei University of Technology, Hefei, Anhui 230009, China
[h] The Third Exploration Team of Shandong Coalfield Geologic Bureau, Taian, Shandong 250102, China
[i] Shandong Provincial Lunan Geo-engineering Exploration Instituts, Jining, Shandong 272100, China

A R T I C L E I N F O

Article history:
Received 15 November 2020
Accepted 3 September 2021
Available online 26 January 2022

Edited by Jie Hao and Teng Zhu

Keywords:
Gas occurrence regularity
Effective extraction radius
THM fields and SLG phases
Numerical simulation
COMSOL Multiphysics
Hudi coal mine

A B S T R A C T

The analysis of the coupling mechanism of thermal-hydraulic-mechanical (THM) fields, and solid-liquid-gas (SLG) phases during gas extraction process is of profound significance to explore its numerical application in the gas occurrence regularity and its effective extraction radius. In this study, the Hudi coal mine in Qinshui basin is taken as the research area, the influencing factors of gas occurrence were analyzed, the differences in overburden load for gas pressure distribution and the factors influencing the effective extraction radius were further discussed by using the COMSOL software. The results show that the derivation of mathematical model in gas extraction shows that the process is a process the THM fields restrict each other, and the SLG phases influence each other. The longer the extraction time, the larger the influencing range of borehole, and the better the extraction effect. The larger the diameter of borehole, the larger the effective extraction radius, and the influence on gas extraction effect is smaller in the early stage and larger in the late stage. The borehole arrangement should be flexibly arranged according to the actual extraction situation. The higher the porosity, the higher the permeability, the better the gas extraction effect. The larger the overburden load of reservoir, the stronger the effective stress, which will result in the more severe the strain, and the closure of pore and fracture, which in turn will lead to the decrease of permeability and slow down the gas extraction. The relationship among extraction time, borehole diameter, negative pressure of gas extraction, permeability with effective extraction radius is exponential. This study has important theoretical and practical significance for clarifying and summarizing the gas occurrence regularity and its engineering practice.

1. Introduction

With the increase of mining intensity and depth, the gas emission amount increases, and the proportion of gas accident in coal mining accidents is getting higher and higher (He et al., 2019). The

* Corresponding author.
** Corresponding author.
E-mail addresses: huihuangfang@aust.edu.cn (H.-H. Fang), chunshanzheng@aust.edu.cn (C.-S. Zheng).

https://doi.org/10.1016/j.petsci.2022.01.020
1995-8226/

gas extraction can not only effectively control gas accidents and reduce safety hazards, but also make use of gas as a kind of clean energy (Wang et al., 2018a; Cheng et al., 2020), which is closely related to gas occurrence regularity and effective extraction radius (Cheng et al., 2018; Xu et al., 2020). Therefore, the study of gas occurrence regularity and its effective extraction radius is the key to ensure the safe extraction.

Previous scholars have carried out lots of studies on the gas occurrence regularity. In terms of contents, it mainly discusses the influence of the internal or external factors on the gas occurrence regularity (Du et al., 2020; Ma et al., 2020). As far as theory is concerned, there are mainly linear/nonlinear seepage theory, gas diffusion and seepage theory and gas multi-fields coupling theory (Chen et al., 2017; Qin et al., 2019a). In terms of methods, the numerical and experiment simulation, and engineering and geologic statistics are mainly presented in combination (Du and Wang, 2019; Chen et al., 2020).

The effective extraction radius is an important parameter to determine the borehole arrangement (Qin et al., 2019b), which is directly related to the length of pre-extraction time and the final extraction effect (Zhang et al., 2019a). For coal seam with low extraction efficiency, the research on effective extraction radius should be strengthened to effectively improve gas extraction rate (Chen et al., 2018). The effective extraction radius can be studied by field test and numerical simulation (Wei et al., 2019), and which can be determined by the residual gas content, the residual gas pressure and the relative gas pressure (Tang et al., 2019).

The gas occurrence is a process in which the THM fields restrict each other, and the SLG phases interact each other (Zhao et al. 2018, 2020). The analysis of the coupling mechanism of THM fields and SLG phases during gas extraction process is of profound significance to explore its numerical application in the gas occurrence regularity and its effective extraction radius. The numerical simulation technology is striving to achieve the coupling of THM fields and SLG phases, so as to gradually approach the real geological environment (Rong et al., 2019; Wu et al., 2020).

Previous studies did not consider the relationship between the THM fields and the SLG phases, and the derivation of mathematical model only highlights the evolution law of a certain physical field or a certain phase (Xue, 2017; Wei et al., 2019). Studies on the influence of gas occurrence regularity usually focus on the internal factors or the external factors, and there are few studies on the correlation between the factors (Du et al., 2020; Ma et al., 2020). Therefore, it is very important to deduce the THM fields and SLG phases fully coupled mathematical model with considering the internal and external factors, and explore its numerical application in the gas occurrence regularity and its effective extraction radius under gas extraction process.

In this study, the Hudi coal mine in Qinshui basin is taken as the research area, and the purpose is to analyze the full coupling mechanism of THM fields and SLG phases, and explore its numerical application in the gas occurrence regularity and its effective extraction radius during gas extraction process. By using the COMSOL Multiphysics software (*www.comsol.com*), the influencing factors of gas occurrence regularity were analyzed, the differences in overburden load for gas pressure distribution and the factors influencing the effective extraction radius were further discussed. The innovations of this study are shown as follows: ① The fully coupled mathematical model of THM fields and the SLG phases is derived. ②The influence of engineering factors and geological factors on gas occurrence regularity is quantitatively analyzed. ③The differences of overburden load for gas pressure distribution are discussed. ④The influences of the extraction time, the borehole diameter, the negative pressure of gas extraction, and the permeability on the effective extraction radius are discussed. This study has important theoretical and practical significance for clarifying and summarizing the gas occurrence regularity and its engineering practice.

2. Derivation and verification of the THM fields and SLG phases fully coupled model

2.1. Basic assumptions

In order to reveal the coupling mechanism of THM fields and SLG phases and further deduce the fully coupled mathematical model during gas extraction process, the following assumptions are proposed (Duan et al., 2019; Huo et al., 2019; Wang et al., 2019; Wei et al., 2019; Zhang et al., 2019b; Qin et al., 2020): ①The coal seam is a uniform and isotropic continuous medium, that is, the pore and fracture structure of coal seam is uniform on the macro scale, the physical properties are the same everywhere, and the coal parameters are equally isotropic. ②The coal seam is a linear elastic object, and coal deformation in the extraction process is small, so it can be considered that the coal seam is in the stage of elastic deformation which can be recovered, so that the stress and strain have a unique corresponding relationship. ③The coal seam is a double structure of pore and fracture. The surface of pore and fracture is the main place for gas adsorption, and the gas migration is mainly along the large pore and fracture, which conforms to Darcy's Law. ④Gas exists in coal seam in free and adsorbed states, which obey the ideal gas equation and the modified Langmuir equation, respectively. ⑤Pores are only saturated with gas phase, and the fractures are saturated with gas and water phases.

2.2. Derivation of the fully coupled mathematical model

2.2.1. Governing equation of mechanical field

By analyzing the strain caused by the thermal expansion/contraction, the reservoir pressure in pore and fracture systems, and the gas desorption/adsorption (Wang et al., 2018b; Xue et al., 2018; Li et al., 2020), the constitutive equation of mechanical field in non-isothermal coal reservoir can be derived, which can be expressed as follows:

$$\varepsilon_{ij}=\frac{1}{2G}\sigma_{ij}-\left(\frac{1}{6G}-\frac{1}{9K}\right)\sigma_{kk}\delta_{ij}+\frac{\alpha_T}{3}(T-T_0)\delta_{ij}+\frac{\alpha_m P_m+\alpha_f P_f}{3}\delta_{ij}+\frac{\varepsilon_a}{3}\delta_{ij} \tag{1}$$

where,

$$G=D/[2\cdot(1+\nu)] \tag{2}$$

$$D=1\Big/\left(1\Big/E+1\Big/K_f\right) \tag{3}$$

$$K=D/[3\cdot(1-2\nu)] \tag{4}$$

$$K_m=E_m/[3\cdot(1-2\nu)] \tag{5}$$

$$\varepsilon_a=\alpha_{sg}\cdot V_{sg} \tag{6}$$

$$\alpha_m=1-K/K_m \tag{7}$$

$$\alpha_f=1-K\Big/K_f \tag{8}$$

where, G is the shear modulus, Pa; K is the volume modulus, Pa; α_T is the thermal expansion coefficient, K^{-1}; T is the temperature variable, K; T_0 is the initial temperature, K; α_m and α_f are the Biot effective pressure coefficients in matrix and fracture systems, respectively. P_f is the mixing pressure of gas and water phases in fracture system, Pa; P_m is the gas pressure in matrix system, Pa; ε_a is the matrix contraction strain induced by gas desorption; D is the effective elastic modulus, Pa; v is the Poisson's ratio; E is the elastic modulus, Pa; K_f is the volume elastic modulus in fracture system, Pa; K_m is the volume elastic modulus in matrix system, Pa; E_m is the elastic modulus in matrix system, Pa; α_{sg} is the induced strain coefficient of gas adsorption, kg/m^3; and V_{sg} is the content of adsorbed gas, m^3/kg.

The gas pressure in fracture system can be expressed as follows (Li et al., 2016; Fan et al., 2017):

$$P_f = S_w P_{fw} + S_g P_{fg} \tag{9}$$

where,

$$S_w = (1 - S_{gr} - S_{wr})\left(\frac{P_{cgw}}{P_m + P_{fg} - P_{fw}}\right)\gamma + S_{wr} \tag{10}$$

$$P_{cgw} = P_{fg} - P_{fw} \tag{11}$$

$$S_w + S_g = 1 \tag{12}$$

where, S_w is the saturation of water phase; P_{fw} is the water phase pressure in fracture system, Pa; S_g is the saturation of gas phase; P_{fg} is the gas phase pressure in fracture system, Pa; S_{gr} is the saturation of residual gas phase; S_{wr} is the saturation of residual water phase; P_{cgw} is the capillary pressure; and γ is the aperture distribution index.

The content of adsorbed gas follows the modified Langmuir volume equation (Li et al., 2016; Connell et al., 2019), which can be expressed as follows:

$$V_{sg} = \frac{V_L P_m}{P_L + P_m}\exp\left[-\frac{d_1}{1 + d_2 P_m}(T - T_t)\right] \tag{13}$$

where, d_1 is the pressure coefficient, Pa^{-1}; d_2 is the temperature coefficient, K^{-1}; V_L is the Langmuir volume constant, m^3/kg; P_L is the Langmuir pressure constant, Pa; and T_t is the referencing temperature of adsorption/desorption experiment of coal, K.

The Cauchy's law mainly represents the relationship between reservoir strain and displacement (Fei et al., 2020; Wang et al., 2020), which can be expressed as follows:

$$2\varepsilon_{ij} - u_{i,j} - u_{j,i} = 0 \tag{14}$$

where, μ_i is the reservoir displacement in the i direction.

The stress balance equation can be expressed as follows (Sang et al., 2016; Cui et al., 2018; Fan et al., 2018):

$$\sigma_{ij,j} = -f_i \tag{15}$$

where, f_i is the volume stress of reservoir in the i direction.

In summary, the improved mechanical field equation during gas extraction process can be defined based on Equations 1–15, which are expressed as follows:

$$Gu_{i,jj} + \frac{G}{1-2v}u_{j,ji} - K\alpha_T T_i - \alpha_m P_{m,i} - \alpha_f P_{f,i} - K\varepsilon_{a,i} + f_i = 0 \tag{16}$$

2.2.2. Governing equation of hydrological field in matrix system

The gas in matrix system is mainly adsorbed and free state, and its gas content can be expressed as follows (Ren et al., 2017; Yin et al., 2017; Wang et al., 2018c, 2018d):

$$m_m = V_{sg}\rho_s \frac{M_g}{RT_s}P_s + \varphi_m \frac{M_g}{RT}P_m \tag{17}$$

where, m_m is the gas content in matrix system per unit volume, kg/m^3; V_{sg} is the gas content in adsorbed state, m^3/kg; ρ_s is the coal skeleton density, kg/m^3; M_g is the gas molar mass, kg/mol; R is the gas molar constant; P_s is the standard atmospheric pressure, Pa; T_s is the temperature in normalized state, K; and φ_m stands for the porosity in matrix system.

The gas migration in matrix system is mainly controlled by gas concentration. The gas pressure in matrix system is equal to the gas pressure in fracture system in the original state. When the gas is extracted, the gas adsorbed in matrix system is gradually desorbed to the fracture system due to the differences of gas concentration. According to the Fick's law, the gas mass conservation equation in matrix system can be defined as follows (An et al., 2013; Xia et al., 2015; Li et al., 2016):

$$\frac{\partial m_m}{\partial t} = -\frac{M_g}{\tau RT}\left(P_m - P_{fg}\right) \tag{18}$$

where, τ is the gas desorption time, s.

In summary, the improved hydrological field equation in matrix system during gas extraction process is defined based on Equations (13 and 17-18), which can be expressed as follows:

$$\frac{\partial}{\partial t}\left\{\frac{V_L P_m}{P_L + P_m}\exp\left[-\frac{d_1}{1 + d_2 P_m}(T - T_t)\right]\rho_s \frac{M_g}{RT_s}P_s + \varphi_m \frac{M_g}{RT}P_m\right\} = -\frac{M_g}{\tau RT}\left(P_m - P_{fg}\right) \tag{19}$$

2.2.3. Governing equation of hydrological field in fracture system

The gas in matrix system provides mass sources for the gas in fracture system during the gas extraction process, so the gas mass conservation equation in fracture system can be defined as follows (Xu et al., 2014; Li et al., 2016):

$$\begin{cases} \dfrac{\partial}{\partial t}\left(S_w \varphi_f \rho_w\right) + \nabla(\rho_w u_w) = 0 \\ \dfrac{\partial}{\partial t}\left(S_g \varphi_f \rho_g\right) + \nabla(\rho_g u_g) = \left(1 - \varphi_f\right)\dfrac{M_g}{\tau RT}\left(P_m - P_{fg}\right) \end{cases} \tag{20}$$

where,φ_f refers to the porosity in fracture system; T is the time, s; u_w is the flow velocity of water phase, m/s; and u_g is the migration velocity of gas phase, m/s.

The density of water phase is closely related to the reservoir temperature, which can be defined as follows:

$$\rho_w = c(T - T_s) + \rho_{ws} \tag{21}$$

where, c is the temperature coefficient of water phase, kg/m^3/K; and ρ_{ws} is the density of water phase with standard state, kg/m^3.

The flow velocity of gas and water phases in fracture system can be defined, respectively, based on the generalized Darcy's law, which can be expressed as follows (Xu et al., 2014; Li et al., 2016):

$$\begin{cases} u_{\mathrm{w}} = \dfrac{kk_{\mathrm{rg0}}k_{\mathrm{rg}}}{\mu_{\mathrm{w}}}\nabla P_{\mathrm{fw}} \\ u_{\mathrm{g}} = \dfrac{kk_{\mathrm{rg0}}k_{\mathrm{rg}}}{\mu_{\mathrm{g}}}\left(1+\dfrac{b_1}{P_{\mathrm{fg}}}\right)\nabla P_{\mathrm{fg}} \end{cases} \tag{22}$$

where, k is the absolute permeability, m^2; k_{rg0} is the endpoint relative permeability of gas phase; k_{rw0} is the endpoint relative permeability of water phase; k_{rg} and k_{rw} are the relative permeability of gas and water phases, respectively; μ_{w} and μ_{g} are the dynamic viscosity of water phase and gas phase, respectively; and b_1 is the Klinkenberg factor, Pa.

The relative permeability of gas and water phases can be defined, respectively, which are expressed as follows (Xu et al., 2014; Li et al., 2016):

$$\begin{cases} k_{\mathrm{rw}} = \left(\dfrac{S_{\mathrm{w}}-S_{\mathrm{wr}}}{1-S_{\mathrm{w}}}\right)^4 \\ k_{\mathrm{rg}} = \left[1-\left(\dfrac{S_{\mathrm{w}}-S_{\mathrm{wr}}}{1-S_{\mathrm{wr}}-S_{\mathrm{gr}}}\right)\right]^2\left[1-\left(\dfrac{S_{\mathrm{w}}-S_{\mathrm{wr}}}{1-S_{\mathrm{wr}}}\right)^2\right] \end{cases} \tag{23}$$

To sum up, the governing equation of hydrological field with water and gas phases in fracture system during gas extraction process can be obtained, respectively, when Equation (21)–(23) is inserted into Equation (20), which can be expressed as follows:

$$\begin{aligned} &\frac{\partial}{\partial t}\left(S_{\mathrm{g}}\varphi_{\mathrm{f}}\frac{M_{\mathrm{g}}}{RT}P_{\mathrm{fg}}\right)+\nabla\left[-\frac{M_{\mathrm{g}}}{RT}\frac{kk_{\mathrm{rg0}}k_{\mathrm{rg}}}{\mu_{\mathrm{g}}}\left(P_{\mathrm{fg}}+b_1\right)\nabla P_{\mathrm{fg}}\right] \\ &=\left(1-\varphi_{\mathrm{f}}\right)\frac{M_{\mathrm{g}}}{\tau RT}\left(P_{\mathrm{m}}-P_{\mathrm{fg}}\right) \end{aligned} \tag{24}$$

$$\begin{aligned} &\frac{\partial}{\partial t}\left\{S_{\mathrm{w}}\varphi_{\mathrm{f}}[c(T-T_{\mathrm{s}})+\rho_{\mathrm{ws}}]\right\}+\nabla\left\{-\left[c(T-T_{\mathrm{s}})\right.\right. \\ &\left.\left.+\rho_{\mathrm{fg}}\right]\frac{kk_{\mathrm{rw0}}k_{\mathrm{rw}}}{\mu_{\mathrm{w}}}\nabla P_{\mathrm{fw}}\right\} \\ &=0 \end{aligned} \tag{25}$$

2.2.4. Governing equation of thermal field

Assuming that the liquid and solid phases are in the thermal equilibrium state, which can be represented by an equation that ignores the thermal energy and the mechanical energy, and the energy can be converted into each other, which can be defined as follows (Lin et al., 2017; Wang et al., 2017; Fan et al., 2018):

$$\begin{aligned} &\frac{\partial}{\partial t}\left[\left(\rho C_{\mathrm{p}}\right)_{\mathrm{eff}}T\right]+\eta_{\mathrm{eff}}\nabla T-\nabla\left(\lambda_{\mathrm{eff}}\nabla T\right)+\alpha_{\mathrm{T}}K_{\mathrm{s}}\frac{\partial\varepsilon_{\mathrm{v}}}{\partial t}+q_{\mathrm{st}}\frac{\rho_{\mathrm{s}}\rho_{\mathrm{gs}}}{M_{\mathrm{g}}}\frac{\partial V_{\mathrm{sg}}}{\partial t} \\ &=0 \end{aligned} \tag{26}$$

The five items on the left side of Equation (26) represent the changes of the internal energy, the heat transfer and conversion, as well as the changes of the strain energy of coal skeleton and the gas adsorption energy, respectively. Among them:

$$\eta_{\mathrm{eff}} = -\frac{kk_{\mathrm{rg0}}k_{\mathrm{rg}}}{\mu_{\mathrm{g}}}\left(1+\frac{b_1}{P_{\mathrm{fg}}}\right)\nabla P_{\mathrm{fg}}\rho_{\mathrm{g}}C_{\mathrm{g}}-\frac{kk_{\mathrm{rw0}}k_{\mathrm{rw}}}{\mu_{\mathrm{w}}}\nabla P_{\mathrm{fw}}\rho_{\mathrm{w}}C_{\mathrm{w}} \tag{27}$$

$$\left(\rho C_{\mathrm{p}}\right)_{\mathrm{eff}} = \left(1-\varphi_{\mathrm{f}}-\varphi_{\mathrm{m}}\right)\rho_{\mathrm{s}}C_{\mathrm{s}}+\left(S_{\mathrm{g}}\varphi_{\mathrm{f}}+\varphi_{\mathrm{m}}\right)\rho_{\mathrm{g}}C_{\mathrm{g}}+S_{\mathrm{w}}\varphi_{\mathrm{f}}\rho_{\mathrm{w}}C_{\mathrm{w}} \tag{28}$$

$$\lambda_{\mathrm{eff}} = \left(1-\varphi_{\mathrm{f}}-\varphi_{\mathrm{m}}\right)\lambda_{\mathrm{s}}+\left(S_{\mathrm{g}}\varphi_{\mathrm{f}}+\varphi_{\mathrm{m}}\right)\lambda_{\mathrm{g}}+S_{\mathrm{w}}\varphi_{\mathrm{f}}\lambda_{\mathrm{w}} \tag{29}$$

where, C_{g}, C_{w} and C_{s} are the specific heat capacity of gas phase, liquid phase and reservoir skeleton, respectively, J/kg/K; λ_{g}, λ_{w} and λ_{s} are the thermal conductivity of gas phase, liquid phase and reservoir skeleton, respectively, w/m/K; and q_{st} is the equal volume adsorption heat, kJ/mol.

2.2.5. Dynamic evolution equation of porosity and permeability

The porosity and permeability are the key factors affecting gas extraction, which are very sensitive to the stress state and the coal property. The porosity in matrix system can be defined as follows (Palmer and Mansoori, 1998; Cui and Bustin, 2005; Zhang et al., 2008; Li et al., 2016):

$$\varphi_{\mathrm{m}} = \frac{1}{(1+S)\varphi_{\mathrm{m0}}}\left[(1+S_0)\varphi_{\mathrm{m0}}+\alpha_{\mathrm{m}}(S-S_0)\right] \tag{30}$$

where,

$$S = \varepsilon_{\mathrm{v}}+P_{\mathrm{m}}/K_{\mathrm{s}}-\alpha_{\mathrm{T}}(T-T_0)-\varepsilon_{\mathrm{a}} \tag{31}$$

$$S_0 = \varepsilon_{\mathrm{v0}}+P_{\mathrm{m0}}/K_{\mathrm{s}}-\varepsilon_{\mathrm{a0}} \tag{32}$$

where, ε_{v} is the reservoir volumetric strain; K_{s} is the elastic modulus of coal skeleton; Subscript "0" represents the initial state of the corresponding variable.

The porosity in fracture system can be defined as follows (Wu et al., 2010a; Li et al., 2016):

$$\varphi_{\mathrm{f}} = \varphi_{\mathrm{f0}}-\frac{3\varphi_{\mathrm{f0}}}{\varphi_{\mathrm{f0}}+3K_{\mathrm{f}}/K}\left[\alpha_{\mathrm{T}}(T-T_0)+(\varepsilon_{\mathrm{a}}-\varepsilon_{\mathrm{a0}})-(\varepsilon_{\mathrm{v}}-\varepsilon_{\mathrm{v0}})\right] \tag{33}$$

There is a cube law between permeability and porosity, so the permeability equation can be defined as follows (Palmer and Mansoori, 1998; Pan and Connell, 2007; Wu et al., 2010b; Li et al., 2016; Wang et al., 2018c, 2018d):

$$k = k_0\left\{1-\frac{3}{\varphi_{\mathrm{f0}}+3K_{\mathrm{f}}/K}\left[\alpha_{\mathrm{T}}(T-T_0)+(\varepsilon_{\mathrm{a}}-\varepsilon_{\mathrm{a0}})-(\varepsilon_{\mathrm{v}}-\varepsilon_{\mathrm{v0}})\right]\right\}^3 \tag{34}$$

where, k_0 is the initial permeability of coal reservoir.

2.2.6. Cross coupling of the THM fields and SLG phases

In summary, Equations (2), (16) and (19)4-26 jointly form the fully coupled mathematical model of the THM fields and SLG phases during gas extraction process. The mechanical field equation contains the effective force term, the gas pressure term, the temperature term and the adsorption term, that is, the change of the effective stress, pressure and temperature and the adsorption and desorption of gas will cause the reservoir deformation. The hydrological field equation includes the porosity and permeability equations expressed in terms of volume strain, gas pressure and reservoir temperature, that is, gas flow is affected by coal deformation. The changes in coal reservoir and pore volume caused by changes in effective stress, gas pressure and adsorption stress will

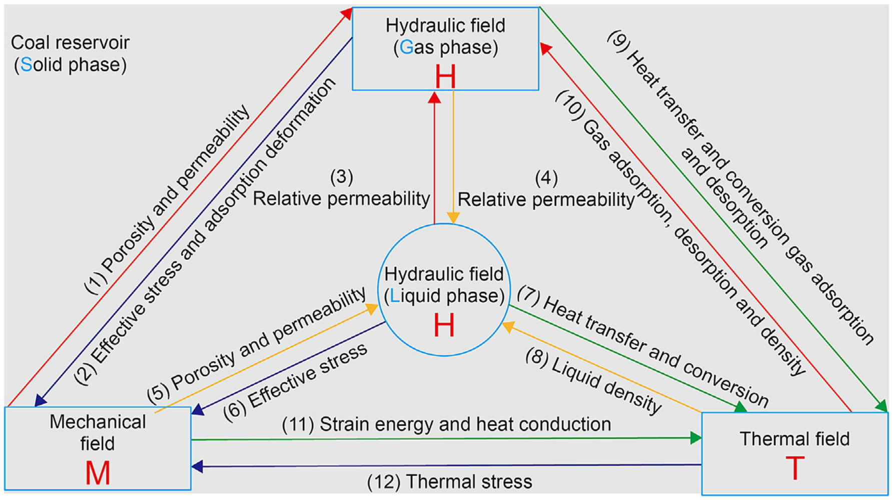

Cross coupled equation

Matrix porosity
$$\phi_m = \frac{1}{(1+S)\phi_{m0}}[(1+S_0)\phi_{m0} + \alpha_m(S-S_0)]$$

Fracture porosity
$$\phi_f = \phi_{f0} - \frac{3\phi_{f0}}{\phi_{f0}+3K_f/K}[\alpha_T(T-T_0)+(\varepsilon_a-\varepsilon_{a0})-(\varepsilon_v-\varepsilon_{v0})]$$

Reservoir permeability
$$k = k_0\left\{1-\frac{3}{\phi_{f0}+3K_f/K}[\alpha_T(T-T_0)+(\varepsilon_a-\varepsilon_{a0})-(\varepsilon_v-\varepsilon_{v0})]\right\}^3$$

Governing equations

Thermal field T
$$\underbrace{\frac{\partial}{\partial t}[(\rho C_p)_{eff}T]}_{(7/9/11)} + \underbrace{\eta_{eff}\nabla T}_{(7/9)} - \underbrace{\nabla(\lambda_{eff}\nabla T)}_{(7/9/11)} + \underbrace{\alpha_T K_s\frac{\partial \varepsilon_v}{\partial t}}_{(11)} + \underbrace{q_{st}\frac{\rho_s\rho_{gs}}{M_g}\frac{\partial V_{sg}}{\partial t}}_{(9)} = 0$$

Hydraulic field H
$$\frac{\partial}{\partial t}\left\{\underbrace{\frac{V_L P_m}{P_L+P_m}\exp[-\frac{d_2}{1+d_1P_m}(T-T_t)]+\rho_s\frac{M_g}{RT_s}P_s}_{(10)}+\underbrace{\phi_m\frac{M_g}{RT}P_m}_{(1/10)}\right\} = \underbrace{-\frac{M_g}{\tau RT}(P_s-P_{fg})}_{(10)}$$
$$\underbrace{\frac{\partial}{\partial t}(S_g\phi_f\frac{M_g}{RT}P_{fg})}_{(1/3/10)} + \nabla[\underbrace{-\frac{M_g}{RT}\frac{kk_{rg0}k_{rg}}{\mu_g}(P_{fg}+b_1)\nabla P_{fg}}_{(1/3/10)}] = \underbrace{(1-\phi_f)\frac{M_g}{\tau RT}(P_m-P_{fg})}_{(10)}$$
$$\frac{\partial}{\partial t}\left\{\underbrace{S_w\phi_f[c(T-T_s)+\rho_{ws}]}_{(4/5/12)}\right\} + \nabla\left\{\underbrace{-[c(T-T_s)+\rho_{fg}]\frac{kk_{rw0}k_{rw}}{\mu_w}\nabla P_{fw}}_{(3/5/8/12)}\right\} = 0$$

Mechanical field M
$$\underbrace{Gu_{i,jj} + \frac{G}{1-2v}u_{j,ji}}_{(1/5/11)} + \underbrace{f_i}_{(1/5/11)} = \underbrace{K\alpha_T T_i}_{(8)} + \underbrace{\alpha_m P_{m,i} + \alpha_f P_{f,i}}_{(2/6)} + \underbrace{K\varepsilon_{a,i}}_{(2)}$$

Fig. 1. The THM fields and SLG phases fully coupled mathematical model during gas extraction process.

change the internal energy of reservoir and gas, which will cause the change of the thermal field. The mathematical model itself is fully coupled (Fig. 1).

The full coupling relationship of THM fields and SLG phases can be expressed as follows: ① The thermal stress caused by the temperature change will have an impact on the mechanical field; ② The strain energy and heat transfer caused by the energy dissipation will affect the reservoir temperature; ③ The change of the gas adsorption, desorption and density caused by temperature change will affect the fluid field; ④ The heat convection and conduction between gas and skeleton, the gas adsorption, and gas desorption will affect the thermal field; ⑤ The change of porosity and permeability caused by reservoir deformation will affect the gas flow; ⑥ The variation of gas pressure will cause reservoir deformation; ⑦ The change of water density caused by temperature change will affect the fluid phase; ⑧ The heat convection and conduction between fluid phase and skeleton will affect the thermal field; ⑨ The change of porosity and permeability caused by reservoir deformation will affect the fluid flow; ⑩ The pressure change of fluid phase will cause reservoir deformation (Fig. 1).

2.3. Verification of the fully coupled mathematical model

Based on the geological background information and the gas extraction data of the Hudi coal mine, the Partial Differential Equation module and the Solid Mechanics module in COMSOL software were used to nest and solve the full coupling equations, so as to verify the accuracy of the mathematical model.

2.3.1. Construction and meshing of geological model

For the coal seam of the 1303 working face in the first mining area of the Hudi coal mine, its occurrence is stable, the average thickness is 5.7 m, the maximum gas content is 15.25 m^3/t, and the maximum gas pressure can reach 2.76 MPa. There are a total of the $1^{\#}$ drilling field on the left and the $2^{\#}$ drilling field on the right of the second lane in this working face (Fig. 2a). In this study, the region with relatively gentle occurrence of coal seam in the left of the first drilling field was selected to establish a

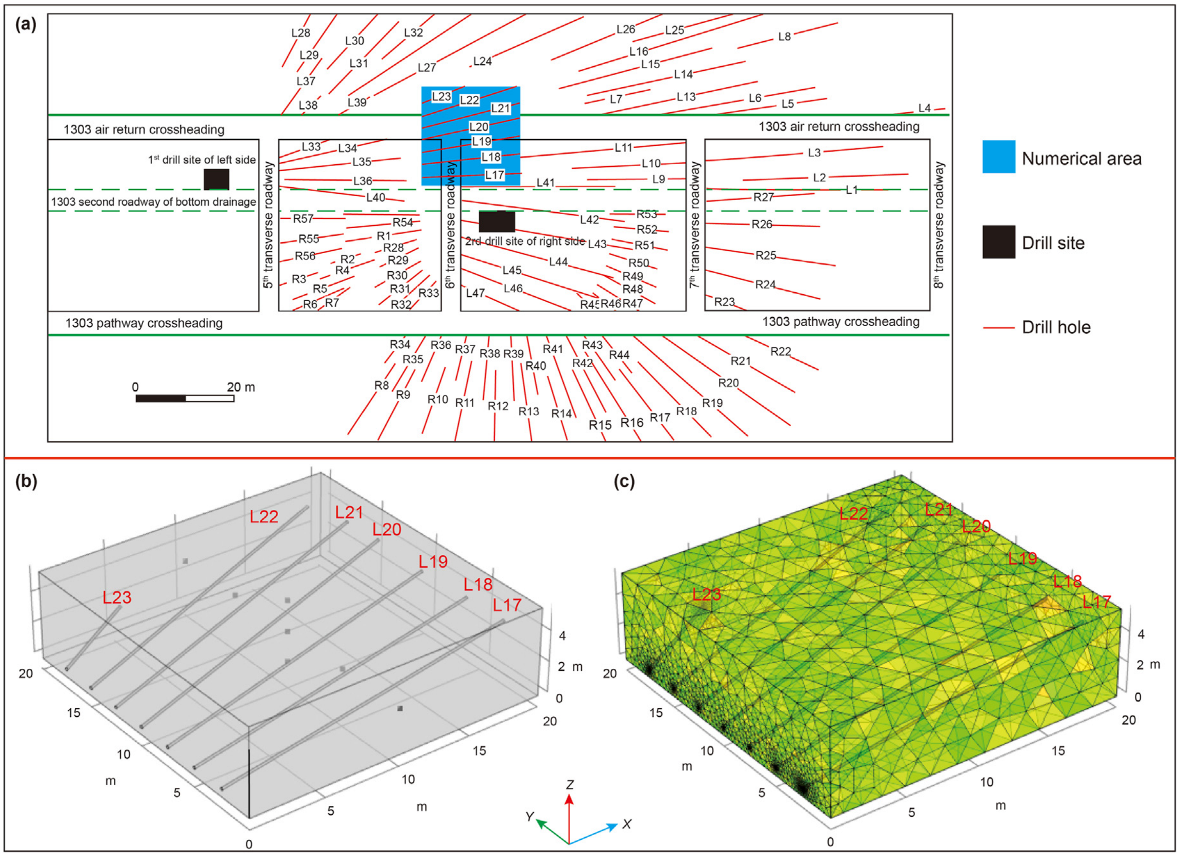

Fig. 2. Construction of geometric model for numerical simulation. (**a**) Borehole layout for 1303 working face; (**b**) Geometric model of numerical simulation; (**c**) Meshing of geometric model.

Table 1
Key parameters of this numerical simulation.

Variable	Parameter	Value (References)	Unit
E	Young's modulus	2.713 (Fan et al., 2018)	GPa
v	Poisson's ratio	0.35 (Lab measurement)	–
E_s	Young's modulus of coal skeleton	8.469 (Fan et al., 2018)	GPa
a	Width in matrix system	0.01 (Lab measurement)	m
b	Opening in fracture system	0.00001 (Lab measurement)	m
α_T	Coefficient of bulk expansion of coal skeleton	2.4e-5 (Fan et al., 2018)	1/K
α_{sg}	Adsorptive strain coefficient	0.06 (Fan et al., 2018)	kg/m^3
ε_L	Langmuir strain coefficient of CH_4	0.0128 (Fan et al., 2019a)	–
P_L	Langmuir pressure coefficient of CH_4	3.034 (Fan et al., 2019a)	MPa
V_L	Langmuir volume coefficient of CH_4	0.036 (Fan et al., 2019a)	m^3/kg
d_1	Temperature coefficient of gas phase	0.02 (Fan et al., 2019a)	1/K
d_2	Pressure coefficient of gas phase	0.07 (Fan et al., 2019a)	1/MPa
T_s	Referencing temperature of gas desorption experiment	273.5 (Lab measurement)	K
φ_m	Porosity in matrix system	0.045 (Lab measurement)	–
φ_f	Porosity in fracture system	0.018 (Lab measurement)	–
k_f	Permeability in fracture system	5.14e-16 (Lab measurement)	m^2
b_1	Gas slippage factor	0.76 (Fan et al., 2018)	MPa
k_{rw0}	Endpoint relative permeability of water phase	1 (Lab measurement)	–
k_{rg0}	Endpoint relative permeability of gas phase	0.756 (Lab measurement)	–
S_{wr}	Saturation of residual water phase	0.52 (Lab measurement)	–
S_{gr}	Saturation of residual gas phase	0.05 (Lab measurement)	–
q_{st}	Equivalent adsorption heat	33.4 (Lab measurement)	kJ/mol
C	Temperature coefficient of water phase	0.0228 (Fan et al., 2018)	$kg/(m^3K)$
λ_s	Thermal conductivity of coal skeleton	0.191 (Fan et al., 2018)	W/m/K
λ_g	Thermal conductivity of gas phase	0.031 (Fan et al., 2018)	W/m/K
λ_w	Thermal conductivity of water phase	0.598 (Fan et al., 2018)	W/m/K
C_s	Specific heat capacity of coal skeleton	1350 (Fan et al., 2018)	J/kg/K
C_g	Specific heat capacity of gas phase	2160 (Fan et al., 2018)	J/kg/K
C_w	Specific heat capacity of water phase	4200 (Fan et al., 2018)	J/kg/K

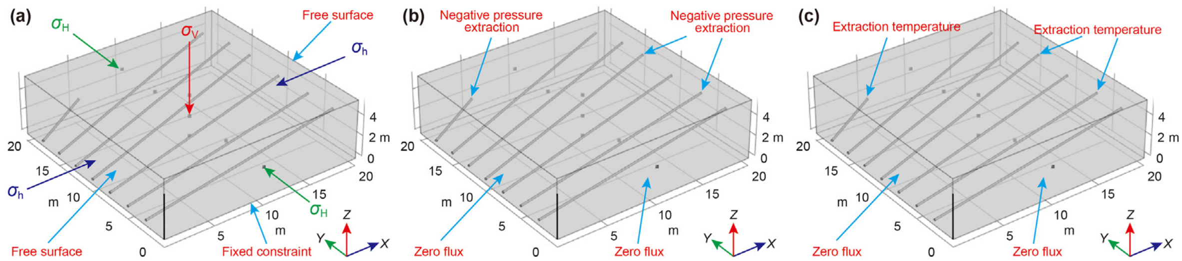

Fig. 3. Boundary condition loading of geological model. (**a**) Mechanical field; (**b**) Hydrological field; (**c**) Thermal field.

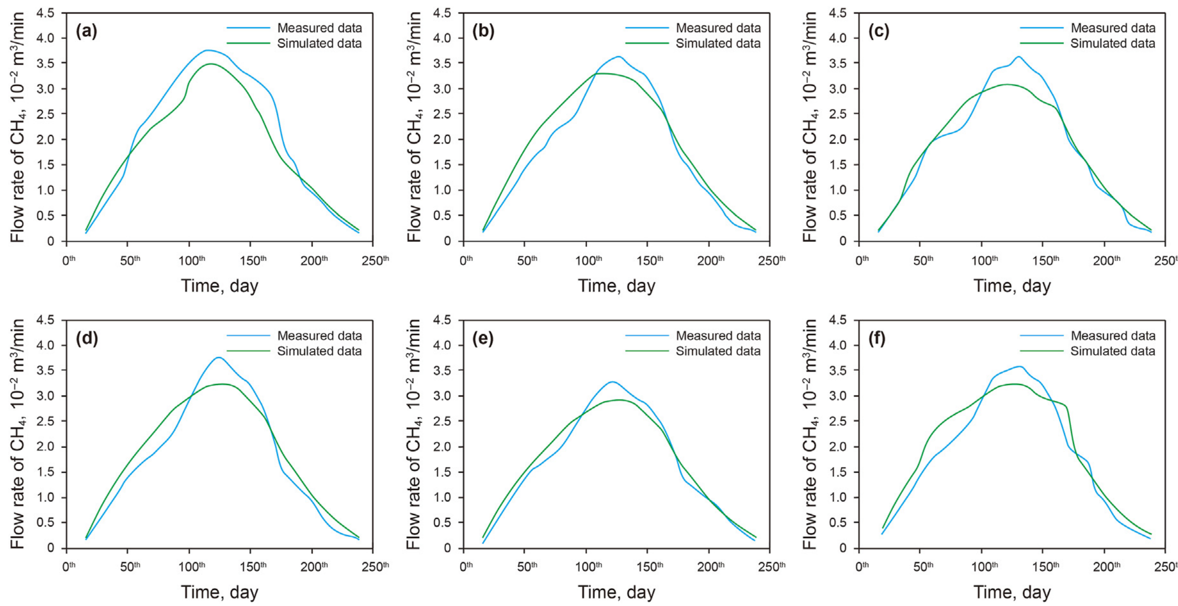

Fig. 4. Comparison between the measured data and the simulated data. (**a**) L17 borehole; (**b**) L18 borehole; (**c**) L19 borehole; (**d**) L20 borehole; (**e**) L21 borehole; (**f**) L22 borehole.

20 m × 20 m × 5.7 m geometric model, and the distribution of borehole was simulated according to the actual borehole location (Fig. 2b).

In this study, grids of different specifications were divided for different parts of the analysis domain. The free triangle sections were refined at the boundary of the borehole, and the free tetrahedral sections were standardized at other locations to simplify the calculation process. The complete grid consisted of 53827 domain elements, 6808 boundary elements and 1770 edge elements (Fig. 2c).

2.3.2. Numerical parameters

This study takes the 3# coal seam in Hudi coal mine as the research object. The numerical parameters were collected from the geological data and the testing data of the coal samples collected from this coal mine (Fan et al., 2018; Fang et al., 2019a, 2019b). The key parameters for this simulation are shown in Table 1.

2.3.3. Definite conditions

Mechanical field: the initial displacement is 0, and the type of mechanical field is analyzed based on the ground stress data, which are as follows: the maximum horizontal principal stress, vertical stress and minimum horizontal principal stress are 18.34 MPa, 16.47 MPa and 9.41 MPa, respectively. The influence of regional tectonic stress on mechanical field is dominant, and the direction of maximum horizontal principal stress is NEE direction. Therefore, the boundary load on the top surface of this geometric model is set as 16.47 MPa and the direction is opposite to the *Z*-axis. The confining pressure is set as 18.34 MPa along the *Y*-axis direction, 9.41 MPa along the *X*-axis direction, and the loading direction of each axis was opposite. The bottom surface is set as a fixed constraint to control the displacement. Other surfaces are set as the free surface condition, that is, this geometric model can freely move (Fig. 3a).

Hydrological field: the initial reservoir pressure is 2.76 MPa, and the borehole boundary is set as the negative pressure boundary. The other boundaries were set as no flux condition, that is, there was no gas flow around the analysis area, and the fluid flow within the analysis area was only simulated. In order to highlight the extraction capacity of each borehole in the analysis area, the influence of other positions is ignored. Moreover, the roof and floor of this coal seam are all compact and continuous mudstone. Therefore, the no flux conditions can be set around the analysis area to simplify the calculation (Fig. 3b).

Thermal field: the initial temperature is 312.5K, the borehole boundary is set as the constant temperature boundary, and the other boundaries are set as no flux condition. That is to say, it is considered that there is no temperature transfer around the analysis domain, and only the temperature transfer within the analysis domain is simulated and analyzed (Fig. 3c).

2.3.4. Verification of the fully coupled model

The accuracy of the fully coupled mathematical model can be verified by comparing the measured data and the simulated data of the L17-L22 borehole with gas extraction data (Fig. 4).

For the gas extraction data, the variation trend of the measured

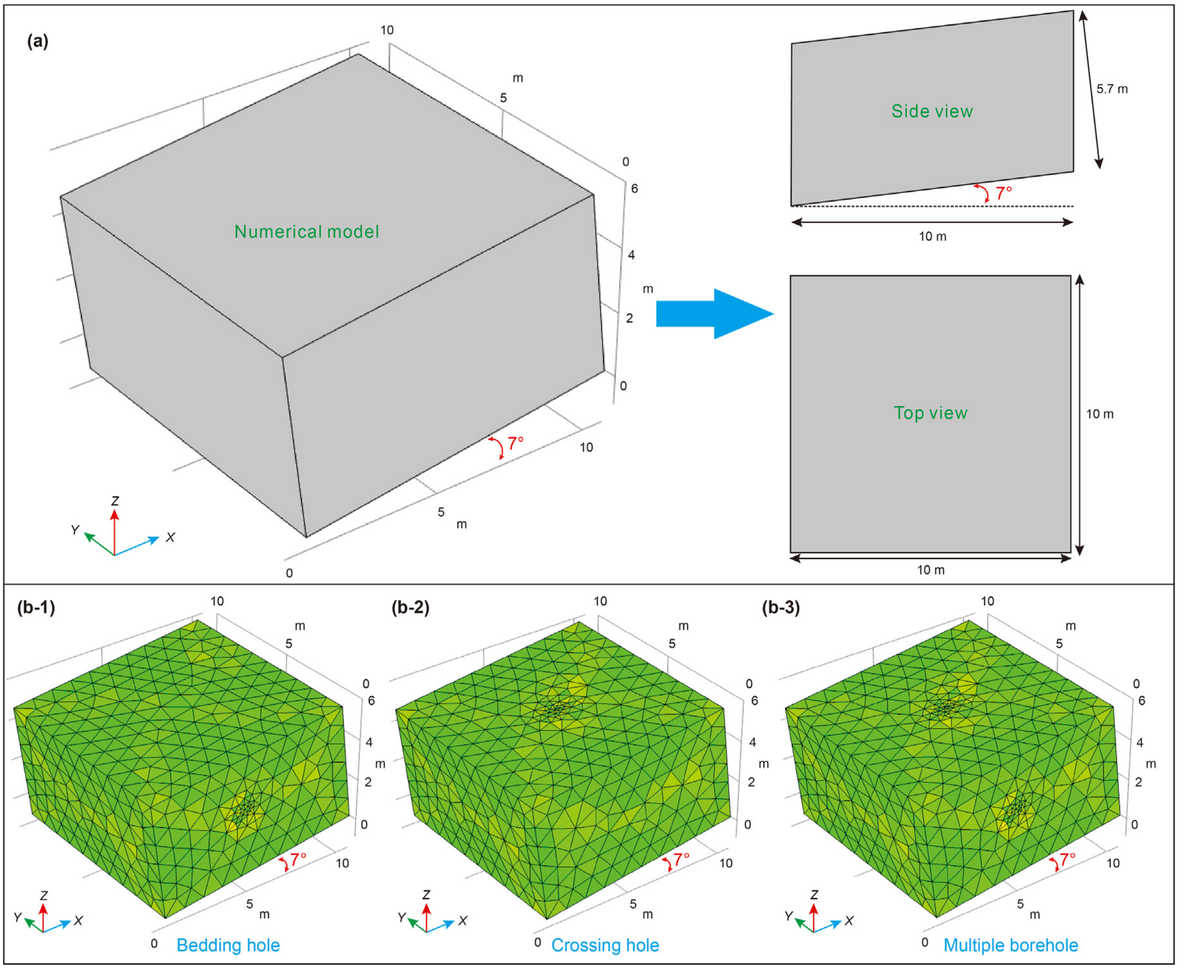

Fig. 5. Geological model and its meshing. (**a**) Geological model and its two views; (**b**-1) Bedding borehole and its meshing; (**b**-2) Crossing borehole and its meshing; (**b**-3) Multiple borehole and its meshing.

Table 2
Numerical schemes of this study.

Numerical schemes	Models	Coupling mode	Influencing factor
A	Model 1: Diameter: 70 mm Model 2: Diameter: 90 mm Model 3: Diameter: 110 mm	THM fields SLG phases	Borehole diameter
B	Model 4: Bedding borehole Model 5: Perforating borehole Model 6: Superposition borehole	THM fields SLG phases	Borehole arrangement
C	Model 7: Porosity: 0.01 Model 8: Porosity: 0.05 Model 9: Porosity: 0.10	THM fields SLG phases	Porosity
D	Model 10: Permeability: 9.1×10^{-15}m^2 Model 11: Permeability: 9.1×10^{-16}m^2 Model 12: Permeability: 9.1×10^{-17}m^2	THM fields SLG phases	Permeability

data is consistent with that of the simulated data, which shows a changing regularity of first increasing and then decreasing, and the maximum error of the gas flow rate at the same time is between 5.41% and 13.83% (Fig. 4). Compared with the measured data, the simulated data is more stable and gentle. The measured data is controlled by engineering factors and geological factors, and the data has a large fluctuation, while the boundary conditions and its coupling factors are relatively stable during the simulation process, so the simulated data is relatively stable. The good consistency between the simulated data and the measured data indicates that the established fully coupled mathematical model can represent the gas flow change of the borehole, and it can be judged that the established fully coupled mathematical model can conform to the actual gas extraction regularity.

3. Geological model and numerical schemes

3.1. Geological model and its meshes

The overall undulations of the 3$^{\#}$ coal seam in Hudi coal mine

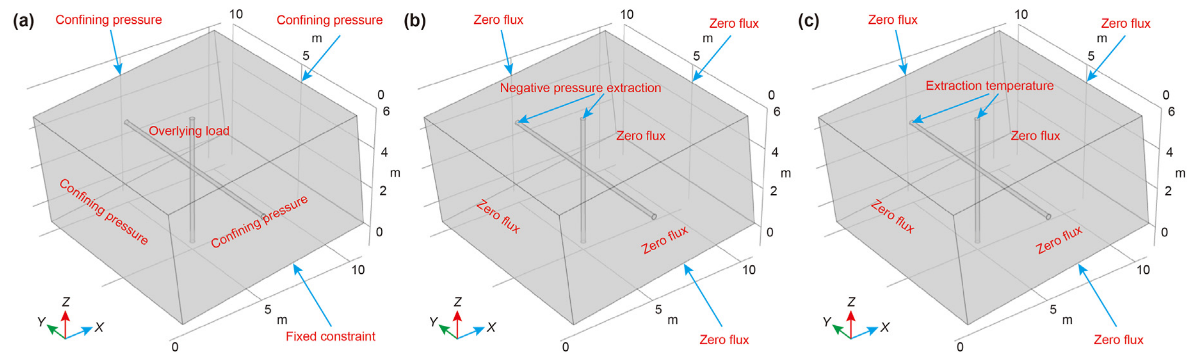

Fig. 6. Boundary condition loading of geological model—a case study of the multiple borehole. (**a**) Mechanical field; (**b**) Hydrological field; (**c**) Thermal field.

are small, and the maximum dip angle is 7°–20°. In order to be closer to the actual geological situation, a tilt model of a rectangle with cross-section of 10 m × 10 m and thickness of 5.7 m was established by referring to the distribution of coal seam and the arrangement of borehole in 1303 working face (Fig. 2; Fig. 5). Boreholes were arranged in vertical, horizontal and multiple forms. Monitoring points were buried at different positions and depths of the model to monitor the dynamic changes of gas extraction. The coordinates of monitoring points with different depths are A_1(7.5,5,3), A_2(7.5,5,4) and A_3(7.5,5,5), respectively. The coordinates of monitoring points with different lengths are B_1(5,5,5)、B_2(5.5,5,5)、B_3(6,5,5)、B_4(6.5,5,5)、B_5(7,5,5)、B_6(7.5,5,5)、B_7(8,5,5)、B_8(8.5,5,5)、B_9(9,5,5)、B_{10}(9.5,5,5), respectively.

The drilling site was divided into the refined free triangular mesh, while the other parts were divided into the standard free tetrahedral mesh, and a total of 21,664 mesh domains were divided (Fig. 5).

3.2. Numerical parameters

As the geological model is constructed by referring to the distribution of coal seam in 1303 working face and the arrangement of borehole, the numerical parameters of this part are adopted the same parameters as those in Section 2.3.2 to better meet the actual gas extraction demand.

3.3. Numerical schemes

The dynamic distribution of gas occurrence is the key to evaluate the gas extraction effect. In addition to the geological influences, the engineering factors cannot be ignored. The engineering factors include the extraction time, borehole diameter, negative pressure of gas extraction and the borehole arrangement. The geological factors include porosity, permeability and initial pressure. Through the method of controlling variables, the influencing characteristics of each factor on gas occurrence were discussed, and then the gas occurrence regularity was obtained (Table 2).

Scheme A, B, C, and D mainly discusses the influence of borehole diameter, borehole arrangement, porosity, and permeability on gas occurrence. respectively (Table 2).

3.4. Definite conditions

In order to better reduce the actual situation of gas extraction and analyze the influence of different influencing factors on the gas occurrence, the boundary conditions of model are idealized to highlight the role of a single factor. The specific boundary conditions can be shown in Fig. 6.

Mechanical field: the mechanical field can be modified and embedded under the Solid Mechanic module in COMSOL software, and the initial displacement is set as 0. The boundary conditions of this model are mainly realized by adding boundary loads. In order to simplify calculation and control variables, loads of the same size and the different directions were added around the analysis field. The top surface of the model can be subjected to an overburden while a load along the *X* axis with positive direction can be added. The bottom surface of the model is a fixed constraint boundary, that is, the location of the analysis domain is fixed, and no displacement or deformation occurs (Fig. 6a).

Hydrological field: the mathematical model is nested under the Mathematical module in COMSOL software, and the initial reservoir pressure can be set in the equation. The boundary condition needs to be realized by adding the Dieldahl-Newman condition. The negative pressure of gas extraction was represented by adding the Dieldahl condition at the borehole boundary, and other boundaries

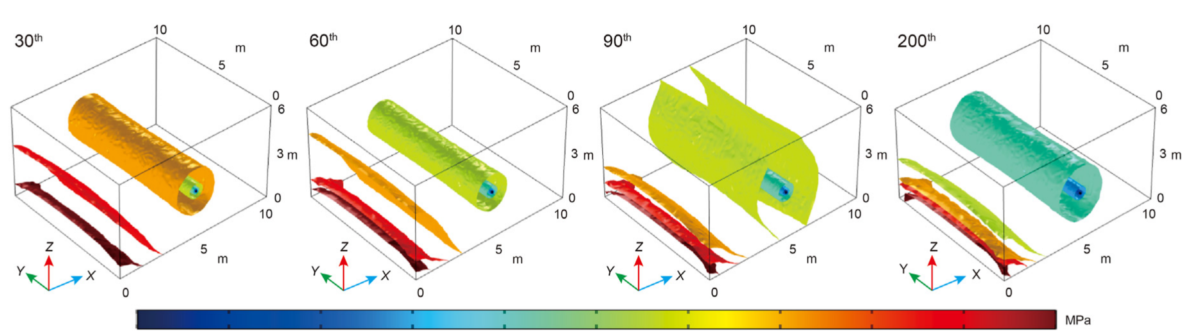

Fig. 7. Isosurface and cloud map of gas pressure at different gas extraction times.

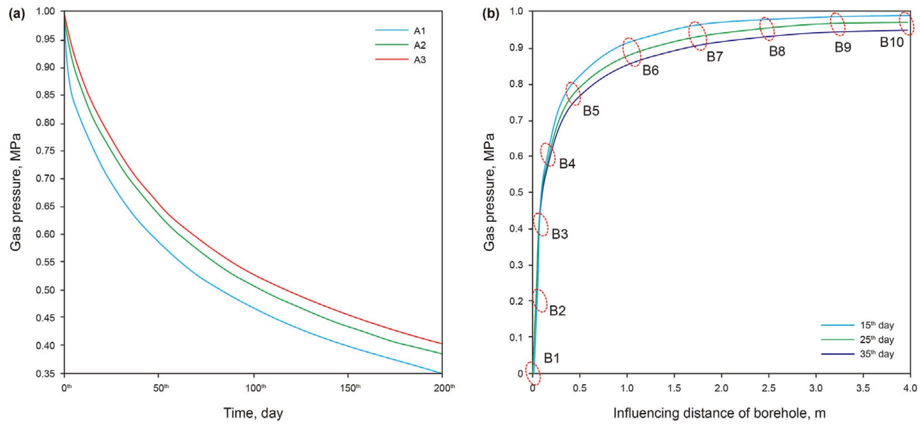

Fig. 8. Variation distribution of gas pressure. (**a**) Variation curves of gas pressure at different depths; (**b**) Variation curves of gas pressure at different lengths.

were set as zero flux condition. That is, the analysis domain was considered to be independent and only the gas dynamic change within the analysis domain was analyzed (Fig. 6b).

Thermal field: the mathematical model is nested under the Mathematical module in COMSOL software, and the initial reservoir temperature is 312.5K, the borehole boundary is set as the constant temperature boundary, and the other boundaries are set as no flux condition. That is to say, it is considered that there is no temperature transfer around the analysis domain (Fig. 6c).

4. Results

4.1. Influence of gas extraction time on gas occurrence regularity

Under the condition that the borehole was arranged in horizontal form and other influencing factors remain unchanged, the dynamic change of reservoir pressure during the gas extraction process is simulated with the initial pressure of 1 MPa and the extraction time of within 200 days. The overall gas extraction effect can be shown in Fig. 7.

The isosurface of gas pressure with borehole as the central axis diffuses to other parts of the analysis domain in an uneven page shape, and the change of color on the isosurface shows the change of gas pressure (Fig. 7). In the initial stage of gas extraction, the scope of borehole action is limited to the vicinity of borehole. With the passage of gas extraction time, the isosurface gradually diffuses to the outside of the borehole, and at the same time, the pressure difference transfers to the periphery of borehole, so that the influencing range is gradually expand. The reservoir pressure is lower on one side of the isosurface near the borebore and higher on the other. According to the Darcy's law, the pressure difference is the main driving force of gas extraction.

In order to better reflect the changes of gas pressure in different regions, the monitoring points with different depths (Point A series) and different lengths (Point B series) were selected to carry out the detection of gas pressure (Fig. 8).

The overall reduction trend of gas pressure at all monitoring points is consistent (Fig. 8a). In the early stage of gas extraction, the curve slope is larger, the gas migration rate is faster, the gas pressure greatly changes, and the changing rate of gas gradually decreases as the gas extraction time goes on. The change of migration rate is mainly controlled by pressure gradient. The initial pressure gradient is large and the gas pressure changes relatively quickly. With the development of gas extraction, the effective range of borehole is expanded, the gas pressure decreases as a whole, which results in the decrease of pressure gradient. Meanwhile, the declining rate of the top measuring point is faster than that of the bottom measuring point. Due to the overburden on the lower part, there is a stress concentration area, in addition, it is also affected by the coal gravity, so the permeability is relatively small. It can be seen from Fig. 8b that with the increase of the distance between the monitoring point and the borehole, the drop of gas pressure has an obvious lag, which indicates that the effect of the borehole is weakened.

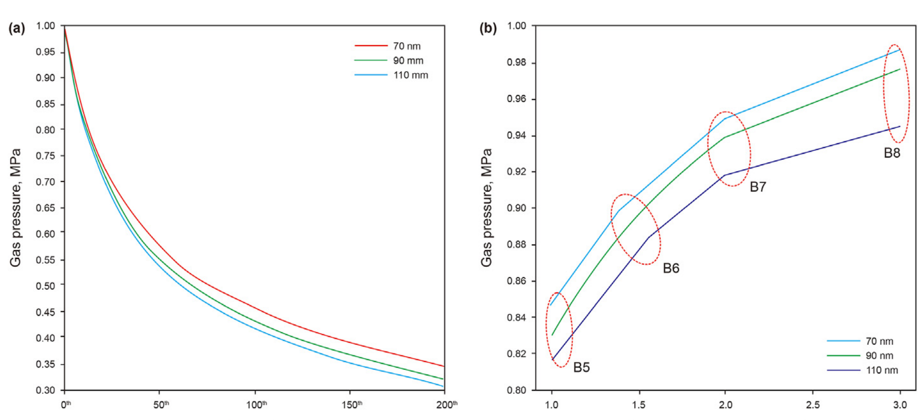

Fig. 9. Gas pressure variation curve with different pore diameter. (**a**) Same location at different times (Point A_2); (**b**) Different location (Point B_3-B_5) at the same time (15th day).

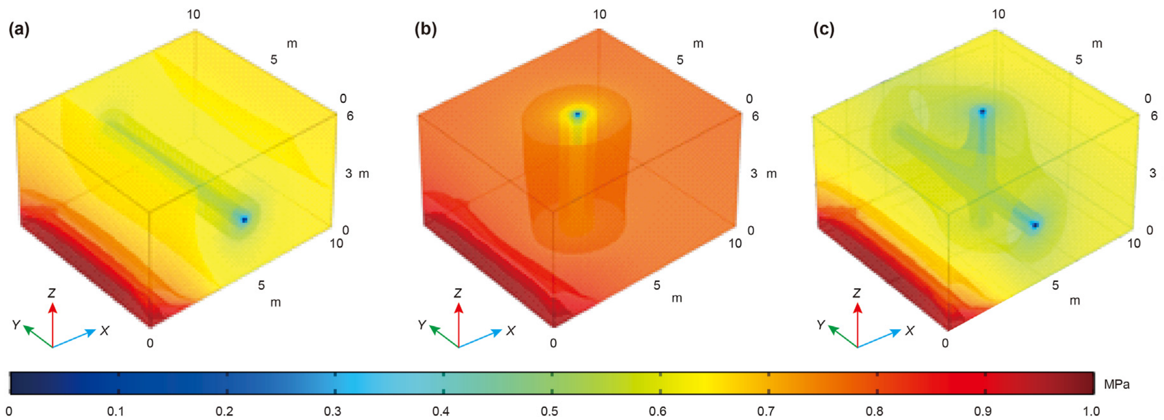

Fig. 10. Cloud map of gas pressure distribution at the same time under different borehole arrangements. (**a**) Bedding borehole; (**b**) Crossing borehole; (**c**) Multiple borehole.

The gas extraction time is the main factor affecting the gas extraction effect, and the extraction time is related to the effective extraction radius. The longer the extraction time, the larger the influencing area of gas extraction. The influence of drilling is relatively weakened on the distal coal seam, which leads to the accumulation of residual gas. Generally speaking, the longer the extraction time, the better the extraction effect and the lower the residual gas content.

4.2. Influence of borehole diameter on gas occurrence regularity

The borehole diameter relates to the design of the extraction borehole, which is controlled by the engineering conditions. In order to increase the comparability, the dynamic change of gas pressure with borehole diameter of 70 mm, 90 mm and 110 mm in the bedding borehole during the gas extraction process were simulated in this study (Fig. 9).

In the early stage of gas extraction, the borehole diameter has little influence on the extraction effect (Fig. 9a). With the development of gas extraction, the influence of borehole diameter becomes more and more obvious. The variation rate of gas pressure increases at the same point, and in the same time, the larger the borehole diameter, the lower the gas pressure. Generally speaking, the larger the borehole diameter is, the larger the exposed area of coal is, and the larger the gas emission will be, which is beneficial to the gas extraction effect. In the early stage of gas extraction, the gas pressure gradient is large, the gas pressure around the borehole rapidly changes, the gas sensitivity to borehole diameter is weak, and the influence of borehole diameter is not obvious. With the passage of gas extraction time, the extraction range is expanded, the larger the borehole diameter is, the larger the relief range of pressure is, and the stronger the influence is on the distal coal seam. Meanwhile, the reduction of pressure difference increases the influence of the borehole diameter. With the increase of borehole diameter, the gas pressure at the monitoring point farther away from the borehole changes more, which conforms to the aforementioned regularity (Fig. 9b).

The influence of borehole diameter on gas dynamic change is mainly reflected in the effective extraction radius. The larger the borehole diameter, the larger the effective extraction radius within the same time.

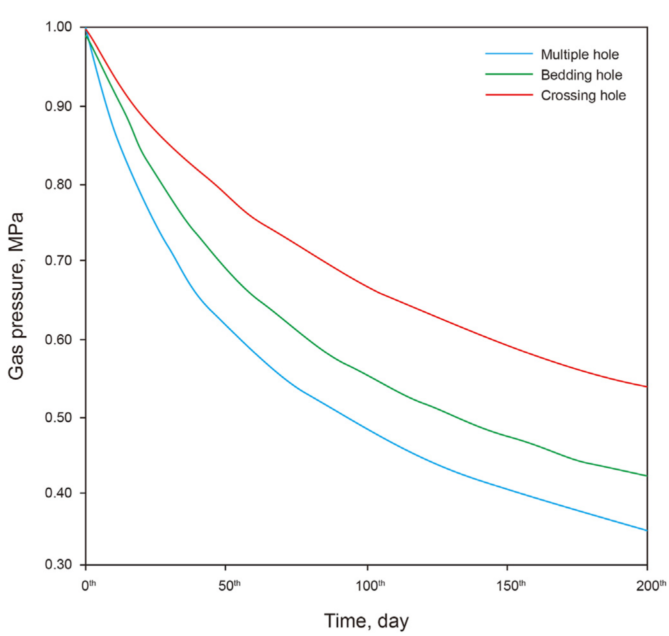

Fig. 11. Variation curves of gas pressure in the same position (A_1) with different arrangement modes.

4.3. Influence of borehole arrangement on gas occurrence regularity

For the same mining block, different borehole arrangements will get different gas extraction effects. In order to explore the influence of borehole arrangement on dynamic change of gas pressure, different arrangements of borehole were added to the prediction model, and the prediction simulation was carried out within 200 days under other conditions were unchanged (Fig. 10).

As far as the overall gas extraction effect is concerned, the gas extraction effect is better if multiple boreholes are jointly arranged, and the gas pressure can drop to a lower state within the same time (Fig. 10).

The gas pressure distribution curve of the same monitoring point (A_1) under different borehole arrangements also shows the same distribution regularity. The gas pressure changes obviously, and the gas variation trend is consistent under the three modes, which shows the characteristic that the changing speed is first fast and then slow. The changing rate of gas is faster in the multiple borehole, the changing gradient of gas pressure is large, and the gas content is the lowest after the same extraction time (Fig. 11).

The isoline of gas pressure in bedding borehole presents asymmetric barrel-shaped diffusion (Fig. 12a). The isoline of gas pressure in crossing borehole show clear funnel shape, the gas pressure in top part of this model quickly drops, while slowly falls

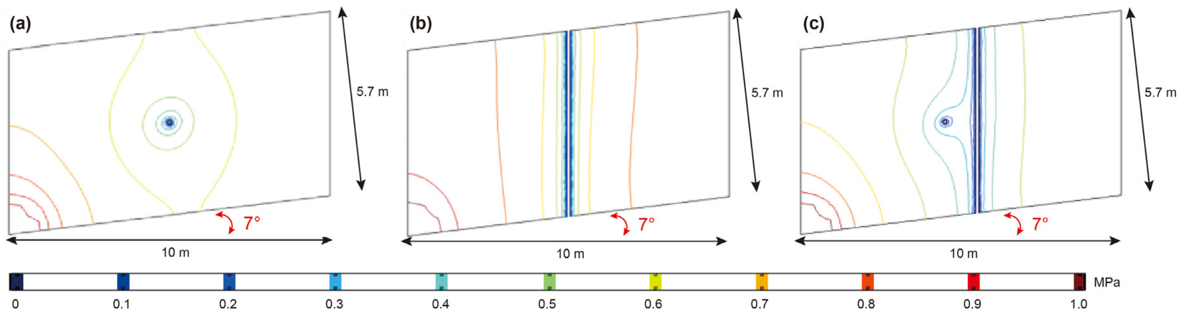

Fig. 12. Contour map of gas pressure on cross sections with different borehole arrangements. (**a**) Bedding borehole; (**b**) Crossing borehole; (**c**) Multiple borehole.

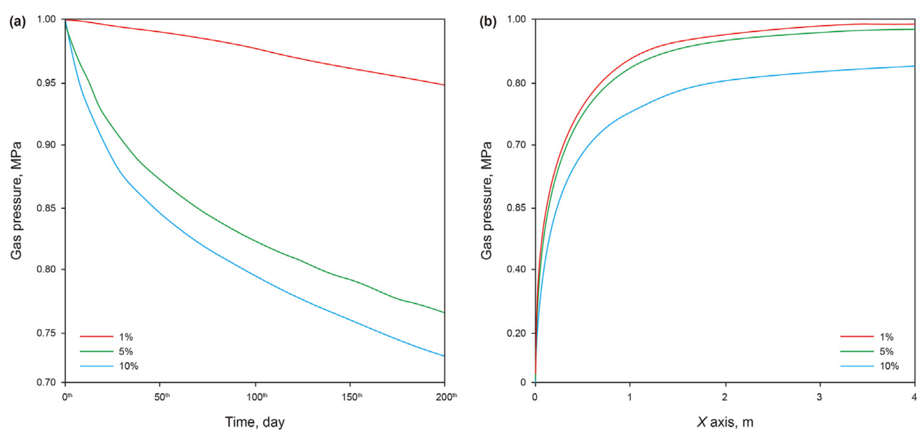

Fig. 13. Gas pressure distribution under different porosity conditions. (**a**) Curve of gas pressure over time; (**b**) Curve of gas pressure with distance from borehole.

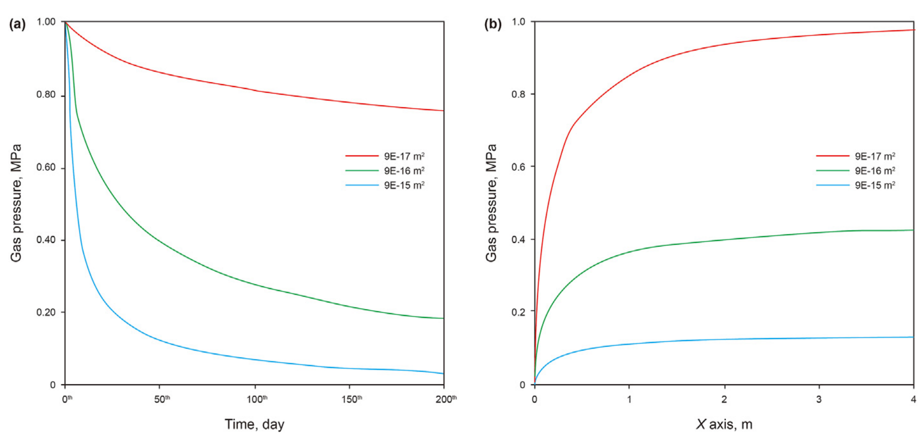

Fig. 14. Gas pressure distribution under different permeability conditions. (**a**) Curves of gas pressure over time; (**b**) Curves of gas pressure with distance from borehole.

at the bottom part (Fig. 12b). Under the overburden load and the coal gravity, the stress condition at the bottom part is concentrated, the permeability is low, the gas flow is blocked, while the relative permeability in top part of this model is high, the gas flow speed is fast, which will result in the isoline of gas pressure presents an asymmetric funnel-shaped distribution. The isoline of gas pressure in multiple borehole has the corresponding morphological characteristics in the other two kinds of borehole arrangements (Fig. 12c). The isoline of gas pressure interfere with each other and form a larger pressure relief range, which is the main reason for its better extraction effect.

The arrangement of borehole is controlled by the engineering conditions. Therefore, although the arrangement of borehole has a great influence on the gas extraction effect, it should be arranged flexibly according to the actual geological situation.

4.4. Influence of porosity and permeability on gas occurrence regularity

Reservoir initial porosity is closely related to permeability. Generally speaking, the greater the porosity, the stronger the permeability, the faster the gas seepage velocity. In order to explore the influence of initial porosity and permeability on the gas dynamic change, the conditions of porosity with 1%, 5% and 10% (Fig. 13) and the permeability of 9.1×10^{-15} m^2, 9.1×10^{-16} m^2, 9.1×10^{-17} m^2 were simulated, respectively (Fig. 14).

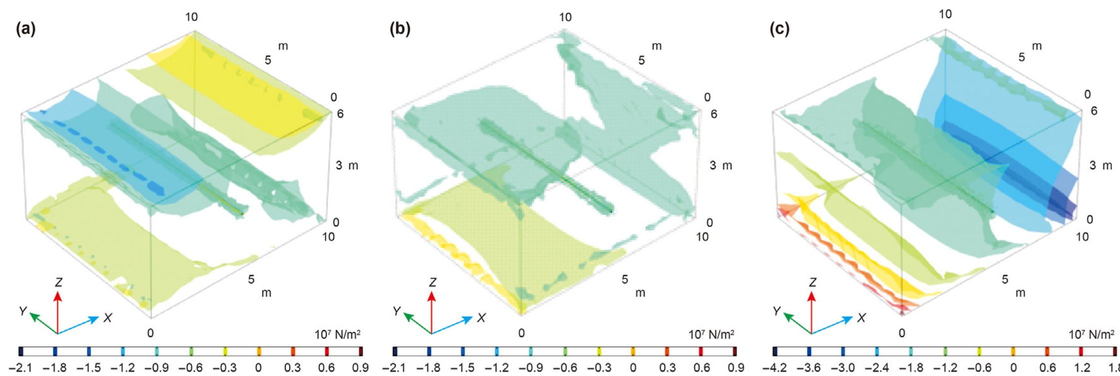

Fig. 15. Isosurface of effective stress component. (**a**) X component of effective pressure; (**b**) Y component of effective pressure; (**c**) Z component of effective pressure.

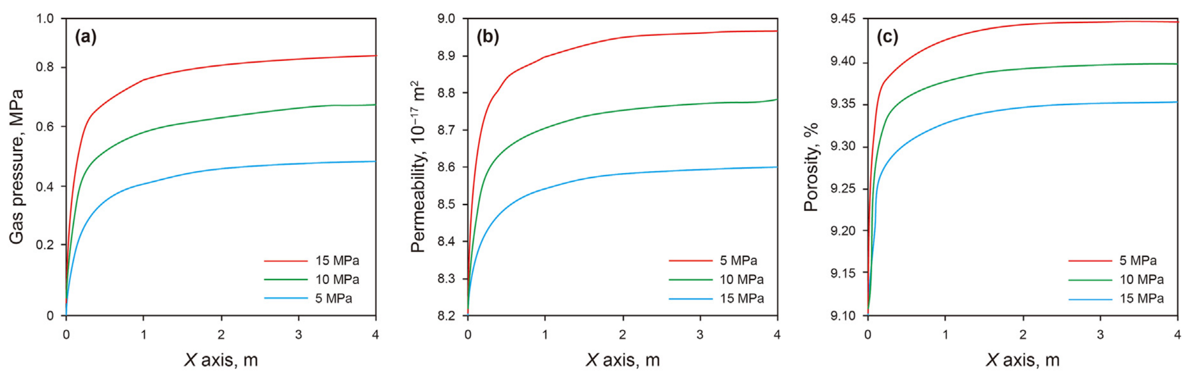

Fig. 16. Influence of overburden load on gas dynamic change. (**a**) Changes in gas pressure; (**b**) Changes in permeability; (**c**) Changes in porosity.

The initial porosity has a significant influence on the change of gas pressure. At the same position, the changing rate of gas pressure increases with the increase of porosity, and when the porosity is smaller, the change of gas pressure has obvious hysteresis (Fig. 13a). The larger the initial porosity is, the larger the influencing range of borehole at the same time period will be (Fig. 13b). The mechanism that porosity affects gas migration is that the porosity is directly related to the permeability. The higher the porosity, the higher the permeability, the faster the gas migration speed and the better the gas extraction effect.

The greater the initial permeability is, the greater the variation of gas pressure at the same monitoring point will be with the increase of extraction time, and the smaller the residual gas pressure will be after the same extraction time (Fig. 14a). With the increase of initial permeability, the gas pressure gradient near the borehole is larger, and the influencing range of the borehole is relatively larger, which leads to an increase in the effective extraction radius of the borehole (Fig. 14b).

The primary reason for the influence of initial permeability on the dynamic change of gas is that the permeability represents the gas migration ability. The higher the initial permeability is, the faster the gas migration will be. In the same time, the gas pressure difference can be transferred to a larger range, which will form a larger pressure relief range, and the better the extraction effect will be. On the contrary, the smaller the initial permeability is, the slower the gas seepage velocity will be, and the worse the gas extraction effect will be. The effect of initial permeability on gas extraction is obvious. For coal seams with high permeability, the gas extraction effect is obvious, while for coal seams with low permeability, the gas extraction effect is poor and residual gas is enriched under the same gas extraction condition.

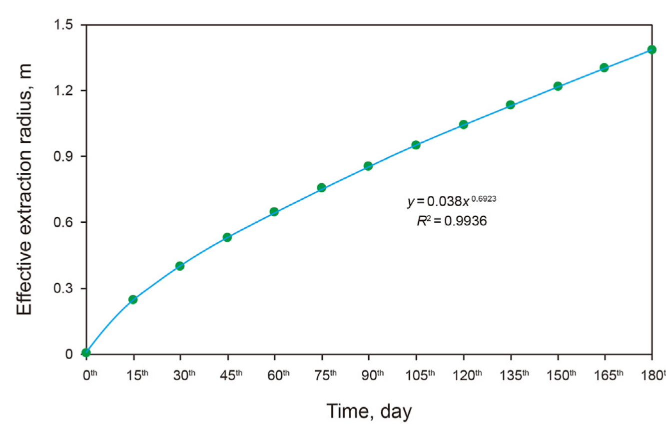

Fig. 17. Change curve of effective extraction radius with gas extraction time.

5. Discussion

5.1. Differences in overburden load of gas pressure distribution

It can be seen from Fig. 7, Figs. 10 and 12 that the gas pressure drops more slowly at the lower part and more quickly at the higher part of the analysis domain. The main reasons for this phenomenon are as follows: under the joint action of the confine pressure and the overburden load, the strain is generated at the different parts of the model, and at the same time, it is also affected by the coal gravity. The lower part of the model is the stress concentration area, the pore and fracture close, the permeability relatively decreases, and the gas pressure slowly drops, which will result in worse gas extraction effect.

The isosurface distribution of principal stress in the analysis domain is shown in Fig. 15. The numerical value in the figure are positive for compressive stress and negative for tensile stress. It can be seen from Fig. 15 that the lower part of the model is all compressive stress under each component, which will lead to the closure of pore and fracture and the decrease of permeability, which is not conducive to the gas extraction.

In order to further explore the regional differences of the isosurface distribution of gas pressure, that is, to explore the influence of overburden load on the dynamic change of gas pressure, the variation of gas pressure within 200 days under 5 MPa, 10 MPa and 15 MPa overburden load was simulated (Fig. 16).

It can be seen from Fig. 16 that the overburden load has a significant influence on the distribution of gas pressure. Within the 60 days of gas extraction in bedding borehole, the gas pressure at the same position decreases with the decrease of the overburden load, which indicates that the overburden load is proportional to the gas pressure. With the increase of overburden load, the permeability and porosity significantly decrease. This is because the greater the buried depth, the greater the overburden load, the stronger the effective stress and the more severe of reservoir strain. The deformation and closure of pore and fracture will lead to the decrease of porosity and permeability and slow down the gas seepage velocity.

5.2. Influencing factors of effective radius for gas extraction

It is pointed out in the Interim Provisions on Coal Mine Gas Drainage Standards (2011 edition) that the determination of whether the drainage standards can be achieved by taking the residual gas pressure as the index can be determined according to the value of 0.74 MPa. Therefore, in this study, the area where the residual gas pressure is lower than 0.74 MPa is defined as the area where the drainage standards are achieved, and the radius of this area is called the effective extraction radius.

5.2.1. Effective extraction radius varies with gas extraction time

In this part, the borehole diameter is 70 mm, the negative pressure of gas extraction is 14 kPa, and the initial permeability is 9.1×10^{-17} m^2. The relationship between the effective extraction radius and the gas extraction time can be simulated and calculated in the bedding borehole, which can be shown in Fig. 17.

Based on the simulated data, the relationship between the effective extraction radius and the gas extraction time can be fitted (Fig. 17). There is a power exponential relationship between the effective extraction radius and the gas extraction time, and the correlation coefficient is as high as 99.9%. The specific mathematical relationship can be shown as follows:

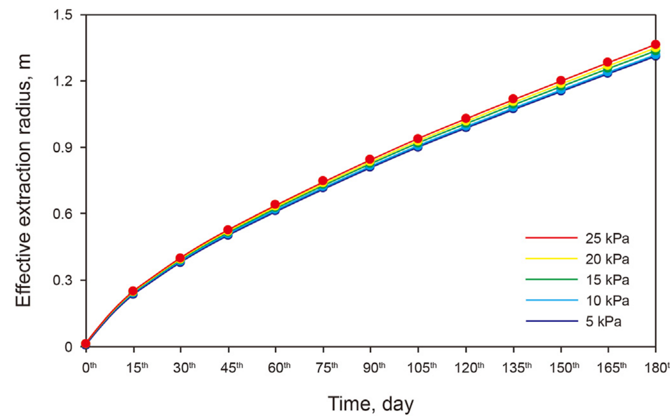

Fig. 19. Changes of effective extraction radius with time under different negative pressures of gas extraction.

$$Y = A_1 X_1^{B_1} = 0.038 X_1^{0.6923} \tag{35}$$

where, Y represents the effective extraction radius, m; A_1 is the time coefficient; B_1 is the time index; and X_1 is the gas extraction time, d.

It can be seen from Fig. 17 that the effective extraction radius increases with the extension of gas extraction time. However, the slope of the curve decreases continuously, which indicates that the increasing amplitude of effective extraction radius decreases.

5.2.2. Effective extraction radius varies with borehole diameter

In this part, the negative pressure of gas extraction is 14 kPa, the initial permeability is 9.1×10^{-17} m^2, and the borehole diameter are selected to be 70 mm, 85 mm, 100 mm, 115 mm and 130 mm, respectively. The effects of different borehole diameters on the effective extraction radius were compared, which are as shown in Fig. 18a. Fig. 18b shows the relationship between the borehole diameter and the effective extraction radius at different gas extraction times.

The larger the borehole diameter, the greater the slope of the curve between the effective extraction radius and the gas extraction time (Fig. 18a). With the increase of borehole diameter, the effective extraction radius continuously increases, and the longer the gas extraction time, the larger the increasing amplitude. On the 30th day of gas extraction, the effective extraction radius of borehole diameter with 100 mm increased by 0.03 m compared with that of borehole diameter with 70 mm, while the difference increased to 0.4 m when the extraction time was 180th day.

Under the condition of different gas extraction times, the effective extraction radius and the borehole diameter all conform to

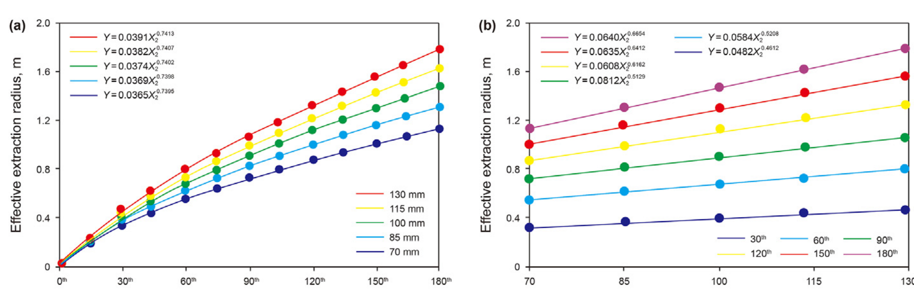

Fig. 18. Schematic diagram of effective extraction radius varying with borehole diameter. (**a**) Changes of effective extraction radius with gas extraction time under different borehole diameters; (**b**) Changes of effective extraction radius with borehole diameter under different gas extraction time.

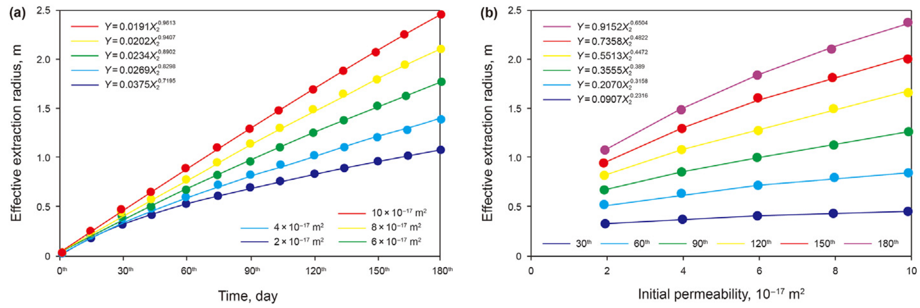

Fig. 20. Schematic diagram of effective extraction radius varying with initial permeability. (**a**) Changes of effective extraction radius with gas extraction time under different initial permeability; (**b**) Changes of effective extraction radius with initial permeability under different gas extraction time.

the power exponential relationship (Fig. 18b), and the correlation coefficient is greater than 0.99, which are as follows:

$$\begin{cases} Y = 0.0640X_2^{0.6654} \\ Y = 0.0635X_2^{0.6412} \\ Y = 0.0608X_2^{0.6162} \\ Y = 0.0812X_2^{0.5129} \\ Y = 0.0584X_2^{0.5208} \\ Y = 0.0482X_2^{0.4612} \end{cases} \tag{36}$$

Therefore, the relationship between the effective extraction radius and the borehole diameter can be obtained as follows:

$$Y = A_2 X_2^{B_2} \tag{37}$$

where, Y is the effective extraction radius, m; X_2 is the borehole diameter, mm; A_2 is the borehole diameter coefficient, which ranges from 0.045 to 0.085. B_2 is the borehole diameter index, and the values range from 0.45 to 0.70.

5.2.3. *Effective extraction radius varies with negative pressure of gas extraction*

In this part, the borehole diameter and the initial permeability are 70 mm and 9.1×10^{-17} m^2, respectively. The negative pressure of gas extraction can be selected with 5 kPa, 10 kPa, 15 kPa, 20 kPa and 25 kPa to simulate the change of the effective extraction radius, and the results are shown in Fig. 19.

Under different negative pressures of gas extraction, the curves almost coincide (Fig. 19). The results show that the effective extraction radius has little change under different negative pressures of gas extraction after the same gas extraction time.

5.2.4. *Effective extraction radius varies with reservoir permeability*

In this part, the negative pressure of gas extraction was 14 kPa, the borehole diameter is 70 mm, and the initial permeability was selected to be 2.0×10^{-17} m^2, 4.0×10^{-17} m^2, 6.0×10^{-17} m^2, 8.0×10^{-17} m^2 and 10.0×10^{-17} m^2, respectively. The effects of different permeability on the effective extraction radius were compared, which are as shown in Fig. 20a. Fig. 20b shows the relationship between the reservoir permeability and the effective extraction radius at different gas extraction times.

The effective extraction radius increases with the increase of initial permeability. The increasing amplitude of effective extraction radius increases with the increase of initial permeability and gas extraction time (Fig. 20a). At the 30th day of gas extraction, the effective extraction radius with the initial permeability of 4.0×10^{-17} m^2 increased by 0.03 m compared with that of 2.0×10^{-17} m^2, while at the 180th day of gas extraction, the difference between the two was 0.4 m.

Under the condition of different extraction times, the relationship of the effective extraction radius and initial permeability all conforms to the power exponential relationship (Fig. 20b), and the correlation coefficient is greater than 0.99, which are as follows:

$$\begin{cases} Y = 0.0907X_2^{0.2316} \\ Y = 0.2070X_2^{0.3158} \\ Y = 0.3555X_2^{0.3890} \\ Y = 0.5513X_2^{0.4472} \\ Y = 0.7358X_2^{0.4822} \\ Y = 0.9152X_2^{0.6504} \end{cases} \tag{38}$$

Therefore, the relationship between the effective extraction radius and initial permeability can be obtained as follows:

$$Y = A_2 X_2^{B_3} \tag{39}$$

where, Y is the effective extraction radius, m; X_3 is the initial permeability, m^2; A_3 is the coefficient of initial permeability, which ranges from 0.09 to 1.00. B_3 is the index of initial permeability, and the values range from 0.20 to 0.70.

6. Conclusion

The purpose of this study is to deduce the fully coupled mathematical model of THM fields and SLG phases during the gas extraction process. The influencing factors of gas occurrence regularity were analyzed, the differences in the overburden load for gas pressure distribution and the factors influencing the effective extraction radius were further discussed. The main conclusions are as follows:

(1) Gas extraction is a process where the thermal field, hydrological field and mechanical field restrict each other, and the solid phase, gas phase and liquid phase influence each other. The derivation of its mathematical model takes into full account the full coupling relationship of each physical field and each phase.
(2) The longer the extraction time, the larger the influencing range of borehole, and the lower the residual gas content. The larger the diameter of borehole, the larger the effective extraction radius, and the influence on gas extraction effect is smaller in the early stage and larger in the late stage. The borehole arrangement should be flexibly arranged according to actual extraction situation. The higher the porosity, the higher the permeability, and the lower the residual gas content.

(3) Gas pressure drops more slowly at the lower part and more quickly at the higher part of the analysis domain. The larger the overburden load of reservoir, the stronger the effective stress of coal, which will result in the more severe the strain, and the deformation and closure of pore and fracture, which in turn will lead to the decrease of permeability and slow down the gas extraction.
(4) There is an exponential relationship among extraction time, borehole diameter, negative pressure of gas extraction, permeability with effective extraction radius. The effective extraction radius increases with the extension of gas extraction time, the increase of borehole diameter and initial permeability, but has little change under different negative pressures of gas extraction.

Acknowledgement

We would like to express our gratitude to the anonymous reviewers for offering their constructive suggestions and comments which improved this manuscript in many aspects. This work was financially supported by the University Synergy Innovation Program of Anhui Province (No. GXXT-2021-018), the National Natural Science Foundation of China (No. 42102217), the Natural Science Research Project of Anhui University (Nos. KJ2020A0315, KJ2020A0317), the Institute of Energy, Hefei Comprehensive National Science Center (No. 21KZS218), the Natural Science Foundation of Anhui Province (No. 2108085MD134), and the Foundation of State Key Laboratory of Petroleum Resources and Prospecting, China University of Petroleum, Beijing (No. PRP/open-2005).

References

An, F.H., Cheng, Y.P., Wang, L., et al., 2013. A numerical model for outburst including the effect of adsorbed gas on coal deformation and mechanical properties. Comput. Geotech. 54, 222–231. https://doi.org/10.1016/j.compgeo.2013.07.013.
Chen, S.K., Yang, T.H., Ranjith, P.G., et al., 2017. Mechanism of the two-phase flow model for water and gas based on adsorption and desorption in fractured coal and rock. Rock Mech. Rock Eng. 50 (3), 571–586. https://doi.org/10.1007/s00603-016-1119-5.
Chen, Y.X., Xu, J., Peng, S.J., et al., 2018. A gas-solid-liquid coupling model of coal seams and the optimization of gas drainage boreholes. Energies 11 (3), 560. https://doi.org/10.3390/en11030560.
Chen, Y.X., Chu, T.X., Chen, X.X., et al., 2020. Coupling of stress and gas pressure in dual porosity medium during coal seam mining. Powder Technol. 367, 390–398. https://doi.org/10.1016/j.powtec.2020.04.009.
Cheng, H.M., Zhang, N., Yang, Y.G., et al., 2018. 3-D dynamic evolution analysis of coal-rock damaged field and gas seepage field during the gas extraction process. J. Nat. Gas Sci. Eng. 56, 444–454. https://doi.org/10.1016/j.jngse.2018.06.015.
Cheng, L., Ge, Z.L., Chen, J.F., et al., 2020. Hydraulic fracturing and its effect on gas extraction and coal and gas outburst prevention in a protective layer: a case study in China. Int. J. Oil Gas Coal Technol. 23 (4), 427–449. https://doi.org/10.1504/IJOGCT.2020.10027850.
Connell, L.D., Pan, Z.J., Camilleri, M., 2019. The variation in produced gas composition from mixed gas coal seam reservoirs. Int. J. Coal Geol. 201, 62–75. https://doi.org/10.1016/j.coal.2018.11.011.
Cui, X., Bustin, R.M., 2005. Volumetric strain associated with methane desorption and its impact on coalbed gas production from deep coal seams. AAPG Bull. 89 (9), 1181–1202. https://doi.org/10.1306/05110504114.
Cui, G.L., Liu, J.S., Wei, M.Y., et al., 2018. Evolution of permeability during the process of shale gas extraction. J. Nat. Gas Sci. Eng. 49, 94–109. https://doi.org/10.1016/j.jngse.2017.10.018.
Du, F., Wang, K., 2019. Unstable failure of gas-bearing coal-rock combination bodies: insights from physical experiments and numerical simulations. Process Saf Environ 129, 264–279. https://doi.org/10.1016/j.psep.2019.06.029.
Du, F., Wang, K., Zhang, X., et al., 2020. Experimental study of coal-gas outburst: insights from coal-rock structure, gas pressure and adsorptivity. Nat. Resour. Res. 29 (4), 2481–2493.
Duan, M.K., Jiang, C.B., Gan, Q., et al., 2020. Study on permeability anisotropy of bedded coal under true triaxial stress and its application. Transport Porous Media 131 (3), 1007–1035. https://doi.org/10.1007/s11242-019-01375-y.
Fan, C.J., Li, S., Luo, M.K., et al., 2017. Coal and gas outburst dynamic system. Int. J. Min. Sci. Technol. 27 (1), 49–55. https://doi.org/10.1016/j.ijmst.2016.11.003.
Fan, Y.P., Deng, C.B., Zhang, X., et al., 2018. Numerical study of CO_2-enhanced coalbed methane recovery. Int J Greenh Gas Con 76, 12–23. https://doi.org/10.1016/j.ijggc.2018.06.016.
Fang, H.H., Sang, S.X., Liu, S.Q., et al., 2019a. Experimental simulation of replacing and displacing CH_4 by injecting supercritical CO_2 and its geological significance. Int. J. Greenh. Gas Control 81, 115–125. https://doi.org/10.1016/j.ijggc.2018.12.015.
Fang, H.H., Sang, S.X., Liu, S.Q., et al., 2019b. Numerical simulation of enhancing coalbed methane recovery by injecting CO_2 with heat injection. Petrol. Sci. 16 (1), 32–43. https://doi.org/10.1007/s12182-018-0291-5.
Fei, Y., Liu, S.Q., Xu, Y.C., et al., 2020. Failure analysis of thin bedrock and clay roof in underground coal mining: case study in Longdong coal mine. Int. J. GeoMech. 20 (10), 04020187. https://doi.org/10.1061/(ASCE)GM.1943-5622.0001839.
He, Z., Wu, Q., Wen, L.J., et al., 2019. A process mining approach to improve emergency rescue processes of fatal gas explosion accidents in Chinese coal mines. Saf. Sci. 111, 154–166. https://doi.org/10.1016/j.ssci.2018.07.006.
Huo, B.J., Jing, X.D., He, A.P., et al., 2019. Hydraulic-mechanical coupling model with dual-porosity dual-permeability for anisotropy coal seams and its application in mine gas extraction. Adv. Civ. Eng. 4534835. https://doi.org/10.1155/2019/4534835, 2019.
Li, S., Fan, C.J., Han, J., et al., 2016. A fully coupled thermal-hydraulic-mechanical model with two-phase flow for coalbed methane extraction. J. Nat. Gas Sci. Eng. 33, 324–336. https://doi.org/10.1016/j.jngse.2016.05.032.
Li, C., Wu, Z., Zhang, W.L., et al., 2020. A case study on asymmetric deformation mechanism of the reserved roadway under mining influences and its control techniques. Geomech Eng 22 (5), 449–460. https://doi.org/10.12989/gae.2020.22.5.449.
Lin, B.Q., Li, H., Chen, Z.Q., et al., 2017. Sensitivity analysis on the microwave heating of coal: a coupled electromagnetic and heat transfer model. Appl. Therm. Eng. 126, 949–962. https://doi.org/10.1016/j.applthermaleng.2017.08.012.
Ma, Y.K., Nie, B.S., He, X.Q., et al., 2020. Mechanism investigation on coal and gas outburst: an overview. Int J Min Met Mater 27 (7), 872–887. https://doi.org/10.1007/s12613-019-1956-9.
Palmer, I., Mansoori, J., 1998. How permeability depends on stress and pore pressure in coal beds: a new model. SPE Reservoir Eval. Eng. 1 (6), 539–544. https://doi.org/10.2118/52607-PA.
Pan, Z.J., Connell, L.D., 2007. A theoretical model for gas adsorption induced coal swelling. Int. J. Coal Geol. 69 (4), 243–252. https://doi.org/10.1016/j.coal.2006.04.006.
Qin, H.J., Wei, J.P., Li, S., 2019a. Analysis of the coal seam spalling-failure mechanism based on the seepage instability theory. PLoS One 14 (7), e0219735. https://doi.org/10.1371/journal.pone.0219735.
Qin, W., Xu, J.L., Hu, G.Z., et al., 2019b. Measurement and simulation study on effective drainage radius of borehole along coal seam. Energy Explor. Exploit. 37 (6), 1657–1679. https://doi.org/10.1177/0144598718787293.
Qin, W., Xu, J.L., Hu, G.Z., 2020. Solid-gas coupling law during methane seepage from a coal mass in the advanced pressure relief area of a mining seam. Int. J. Oil Gas Coal Technol. 23 (1), 106–125. https://doi.org/10.1504/IJOGCT.2020.104971.
Ren, T., Wang, G.D., Cheng, Y.P., et al., 2017. Model development and simulation study of the feasibility of enhancing gas drainage efficiency through nitrogen injection. Fuel 194, 406–422. https://doi.org/10.1016/j.fuel.2017.01.029.
Rong, H., Zhang, H.W., Liang, B., et al., 2019. Analysis of the occurrence mechanism for coal and gas outburst based on multiple discriminant indices. Shock Vib. 7572910. https://doi.org/10.1155/2019/7572910, 2019.
Sang, G.J., Elsworth, D., Miao, X.X., et al., 2016. Numerical study of a stress dependent triple porosity model for shale gas reservoirs accommodating gas diffusion in kerogen. J. Nat. Gas Sci. Eng. 32, 423–438. https://doi.org/10.1016/j.jngse.2016.04.044.
Tang, M.Y., Zheng, P.X., Zheng, C.S., et al., 2019. Numerical analysis and prediction of coal mine methane drainage based on gas-solid coupling model. The Vjesn 26 (3), 752–761. https://doi.org/10.17559/TV-20190224105205.
Wang, J.L., Lian, W.B., Li, P., et al., 2017. Simulation of pyrolysis in low rank coal particle by using DAEM kinetics model: reaction behavior and heat transfer. Fuel 207, 126–135. https://doi.org/10.1016/j.fuel.2017.06.078.
Wang, L., Wang, Z.F., Liu, H., et al., 2018a. An improvement sealing method for gas pressure measurement by drilling a reducing-nipple borehole. Energy Sci Eng 6 (5), 595–606. https://doi.org/10.1002/ese3.235.
Wang, E.Y., Kong, X.G., Hu, S.B., et al., 2018b. Multi-scale fractured coal gas-solid coupling model and its applications in engineering projects. Transport Porous Media 121 (3), 703–724. https://doi.org/10.1007/s11242-017-0981-2.
Wang, G., Wang, K., Jiang, Y.J., et al., 2018c. Reservoir permeability evolution during the process of CO_2-enhanced coalbed methane recovery. Energies 11 (11), 2996. https://doi.org/10.3390/en11112996.
Wang, G., Wang, K., Wang, S.G., et al., 2018d. An improved permeability evolution model and its application in fractured sorbing media. J. Nat. Gas Sci. Eng. 56, 222–232. https://doi.org/10.1016/j.jngse.2018.05.038.
Wang, K., Wang, L., Zhang, X., et al., 2019. Measuring low-rate gas flows of boreholes in coal mines by the needle increasing flow rate method. Energ xplor exploit 37 (5), 1541–1557. https://doi.org/10.1177/0144598719857182.
Wang, B., Zhu, S.T., Jiang, F.X., et al., 2020. Investigating the width of isolated coal pillars in deep hard-strata mines for prevention of mine seismicity and rock burst. Energies 13 (17), 4293. https://doi.org/10.3390/en13174293.
Wei, P., Huang, C.W., Li, X.L., et al., 2019. Numerical simulation of boreholes for gas extraction and effective range of gas extraction in soft coal seams. Energy Sci Eng 7 (5), 1632–1648. https://doi.org/10.1002/ese3.377.
Wu, Y., Liu, J.S., Elsworth, D., et al., 2020a. Dual poroelastic response of a coal seam to CO_2 injection. Int J Greenh Gas Con 4 (4), 668–678. https://doi.org/10.1016/j.ijggc.2010.02.004.

Wu, Y., Liu, J.S., Elsworth, D., et al., 2010. Development of anisotropic permeability during coalbed methane production. J. Nat. Gas Sci. Eng. 2 (4), 197–210. https://doi.org/10.1016/j.jngse.2010.06.002.
Wu, M.Y., Zhang, D.M., Wang, W.S., et al., 2020b. Numerical simulation of hydraulic fracturing based on two-dimensional surface fracture morphology reconstruction and combined finite-discrete element method. J. Nat. Gas Sci. Eng. 82, 103479. https://doi.org/10.1016/j.jngse.2020.103479.
Xia, T.Q., Zhou, F.B., Gao, F., et al., 2015. Simulation of coal self-heating processes in underground methane-rich coal seams. Int. J. Coal Geol. 141–142, 1–12. https://doi.org/10.1016/j.coal.2015.02.007.
Xu, H., Tang, D.Z., Tang, S.H., et al., 2014. A dynamic prediction model for gas-water effective permeability based on coalbed methane production data. Int. J. Coal Geol. 121, 44–52. https://doi.org/10.1016/j.coal.2013.11.008.
Xu, H., Wang, G., Guo, Y.Y., et al., 2020. Theoretical, numerical, and experimental analysis of effective extraction radius of coalbed methane boreholes by a gas seepage model based on defined criteria. Energy Sci Eng 8 (3), 880–897. https://doi.org/10.1002/ese3.557.
Xue, Y., 2017. Numerical simulation of coal deformation and gas flow properties around borehole. Comput. Model. Eng. Sci.: Comp Model Eng. 113 (4), 429–441.
Xue, Y., Dang, F.N., Cao, Z.Z., et al., 2018. Numerical analysis of heat and gas transfer characteristics during heat injection processes based on a thermo-hydro-mechanical model. Energies 11 (7), 1722. https://doi.org/10.3390/en11071722.
Yin, G.Z., Deng, B.Z., Li, M.H., et al., 2017. Impact of injection pressure on CO_2-enhanced coalbed methane recovery considering mass transfer between coal fracture and matrix. Fuel 196, 288–297. https://doi.org/10.1016/j.fuel.2017.02.011.
Zhang, H.B., Liu, J.S., Elsworth, D., 2018. How sorption-induced matrix deformation affects gas flow in coal seams: a new FE model. Int J Rock Mech Min 45 (8), 1226–1236. https://doi.org/10.1016/j.ijrmms.2007.11.007.
Zhang, C.L., Xu, J., Peng, S.J., et al., 2019a. Experimental study of drainage radius considering borehole interaction based on 3D monitoring of gas pressure in coal. Fuel 239, 955–963. https://doi.org/10.1016/j.fuel.2018.11.092.
Zhang, L.H., Lu, G., Chang, C., et al., 2019b. Smulation of a coupled gas flow and geomechanics process in fractured coalbed methane reservoirs. Energy Sci Eng 7 (4), 1095–1105. https://doi.org/10.1002/ese3.322.
Zhao, Y., Lin, B.Q., Liu, T., et al., 2018. Gas flow field evolution around hydraulic slotted borehole in anisotropic coal. J. Nat. Gas Sci. Eng. 58, 189–200. https://doi.org/10.1016/j.jngse.2018.08.006.
Zhao, Y., Lin, B.Q., Liu, T., et al., 2020. Gas flow in hydraulic slotting-disturbed coal seam considering stress relief induced damage. J. Nat. Gas Sci. Eng. 75, 103160. https://doi.org/10.1016/j.jngse.2020.103160.